SCIENTIFIC REPORTS

Correspondence and
requests for materials
should be addressed to
F.Q.H. (huangfq@pku.
edu.cn) or J.H.L. (jhlin@
pku.edu.cn)

New high T_c multiferroics KBiFe$_2$O$_5$ with narrow band gap and promising photovoltaic effect

Ganghua Zhang[1,2], Hui Wu[3,4], Guobao Li[1], Qingzhen Huang[3], Chongyin Yang[2], Fuqiang Huang[1,2], Fuhui Liao[1] & Jianhua Lin[1]

[1]State Key Laboratory of Rare Earth Materials Chemistry and Applications, College of Chemistry and Molecular Engineering, Peking University, Beijing 100871 (P.R. China), [2]CAS Key Laboratory of Materials for Energy Conversion, Shanghai Institute of Ceramics, Chinese Academy of Sciences, Shanghai 200050 (P.R. China), [3]NIST Center for Neutron Research, National Institute of Standards and Technology, Gaithersburg, MD 20899-6102 (USA), [4]Department of Materials Science and Engineering, University of Maryland, College Park, MD 20742 (USA).

Intrinsic polarization of ferroelectrics (FE) helps separate photon-generated charge carriers thus enhances photovoltaic effects. However, traditional FE with transition-metal cations (M) of d^0 electron in MO_6 network typically has a band gap (E_g) exceeding 3.0 eV. Although a smaller E_g (2.6 eV) can be obtained in multiferroic BiFeO$_3$, the value is still too high for optimal solar energy applications. Computational "materials genome" searches have predicted several exotic MO_6 FE with $E_g < 2.0$ eV, all thus far unconfirmed because of synthesis difficulties. Here we report a new FE compound with MO_4 tetrahedral network, KBiFe$_2$O$_5$, which features narrow E_g (1.6 eV), high Curie temperature ($T_c \sim 780$ K) and robust magnetic and photoelectric activities. The high photovoltage (8.8 V) and photocurrent density (15 μA/cm^2) were obtained, which is comparable to the reported BiFeO$_3$. This finding may open a new avenue to discovering and designing optimal FE compounds for solar energy applications.

P hotovoltaic effects in ferroelectrics (FE) have been studied for many decades[1–3]. Recently, the discovery of large photovoltages up to 15 V in multiferroic BiFeO$_3$ films[4] has drawn enormous attention to FE photo-voltaics[5–7]. Different from traditional semiconductor solar cells, the photovoltaic effect in FE is relied on the polarization-induced internal electric field[8–10] (illustrated in Fig. 1a) instead of a p-n or Schottky junctions, which can not only improve the separation and migration of light-generated electron-hole pairs but also reduce the cost of cell fabrication. Moreover, the photo-induced voltages in multidomain ferroelectrics will not be limited to the E_g of light absorbers[10] (see in Supplementary Fig. S1), superior to traditional semiconductor solar cells (<1 V). However, traditional FE are typically insulators of large band gaps (E_g) (supplementary Table S1) with rather limited light absorption and photocurrent, thus unsuitable for photovoltaic applications. Ideally, a photovoltaic material should have[11] (1) a band gap of 1.0–1.8 eV matching the solar spectrum (Fig. 1b and 1c), (2) a large light absorption coefficient of $\sim 10^4$–10^5 cm^{-1} and (3) an intermediate carrier concentration of $\sim 10^{15}$–10^{17} cm^{-3}, in addition to being a polar material with a strong build-in electric field of $\sim 10^4$–10^5 V cm^{-1}. Most FE fail to meet these requirements. For example, BiFeO$_3$, which has attracted much recent attention[4,12], features a relatively low solar cell efficiency ($\sim 3 \times 10^{-3}$%) due to the relatively large band gap (2.6 eV)[13] and the relatively high electrical resistance ($\sim 10^{10}$ Ω cm)[14]. Since light absorption and carrier concentrations are both band-gap dependent, small band gap polar materials are thus of great interest.

To search for such materials, one approach is to rely upon first-principles calculations. Recent studies suggested doping the TiO$_6$ network with an oxygen-vacancy-stabilized d^8 M^{2+} ($M =$ Ni, Pd, Pt, and Ce)[15,16] may lower E_g to below 2.0 eV. Another study suggested increasing tetragonality in Bi(Zn$_{1/2}$Ti$_{1/2}$)O$_3$ and inserting layered B cations may suppress oxygen octahedral rotation thus reducing E_g to 1.48 eV[17]. However, these hypothetical compounds have not been synthesized yet, so whether the predictions will stand is unclear. On the other hand, we note that d^n MO_{6-x} (x being 1 or 2) networks in, e.g., the brownmillerite family (Sr$_2$Fe$_2$O$_5$[18] and Ca$_2$Fe$_2$O$_5$[19], having alternating FeO$_6$ and FeO$_4$) and various cuperates as well as other high T_c superconducting compounds, tend to be good conductors. This suggests that reduced oxygen coordination could offer another strategy to achieve low E_g FE. Indeed, tetrahedral compounds are intrinsically polar because of lack of inversion symmetry. Compared to octahedral compounds, its smaller coordination number and the inverted t_{2g}/e_g orbitals
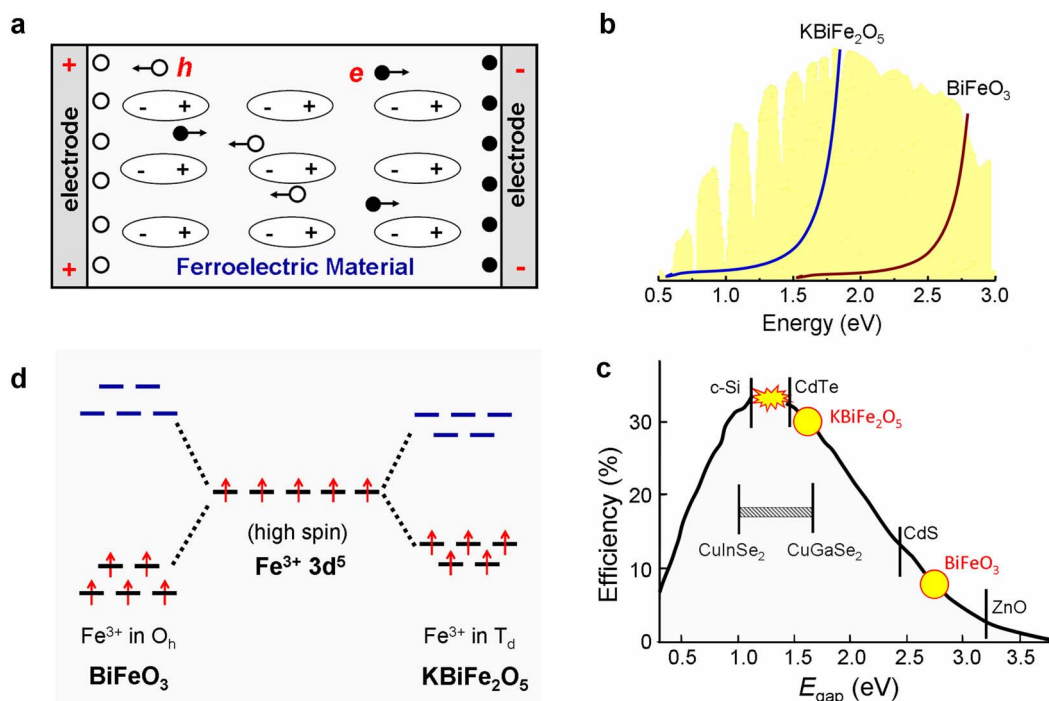
Figure 1 | Selection rules for ferroelectric photovoltaic materials. (a) Schematic illustration of mechanism for photovoltaic effect in ferroelectric materials. (b) Spectra of solar radiance and UV-Vis-near IR absorption of $BiFeO_3$ and $KBiFe_2O_5$. (c) Maximum theoretical efficiency vs. band gap; AM1.5 illumination. (d) Schematic electronic DOS of Fe^{3+} in octahedral O_h and tetrahedral T_d coordination.

should also lead to a smaller E_g (see schematic in Fig. 1d). Yet past studies of tetrahedral structured ferroelectric oxides were limited to main group cations (e.g., $M = P$ as in KH_2PO_4[20] and $M = Ge$ as in $Pb_5Ge_3O_{11}$[21]) or spinels, which tend to have low T_C and/or relative large band gap (supplementary Table S1). In this work, we report a new multiferroic $KBiFe_2O_5$ crystal structure which contains tetrahedral Fe^{3+} in a $[Fe_2O_3]$ block that alternates with a $[(K, Bi)O_2]$ block (Fig. 2). Exploratory characterization of this compound found a much lower $E_g \sim 1.6$ eV and promising dielectric, ferroic and photosensitive properties. It is worth noting that the theoretical photovoltaic efficiency limit of $KBiFe_2O_5$ (~30%) obtained from Fig. 1c

is far beyond $BiFeO_3$ (~7%) according to different solar absorptions, indicating narrow band gap multiferroics possesses great potential applications in optoelectronic and solar energy devices.

Results

Room temperature structure. Single crystal x-ray diffraction (XRD) data of $KBiFe_2O_5$ at room temperature can be fitted using a new crystal structure type of orthorhombic space group $P2_1cn$ with cell parameters $a = 7.9841(5)$ Å, $b = 11.8192(8)$ Å, $c = 5.7393(4)$ Å and $Z = 4$. (See results of structure refinement in supporting information Tables S2 and S3.) Each unit cell contains one crystallographically independent K and Bi, two Fe, and five O (Supplementary Table S3 and Fig. 2a). Each Fe forms a distorted oxygen tetrahedron with four Fe-O bonds in the range of 1.801–1.916 Å, which are shorter than six Fe–O bonds in $BiFeO_3$[22]. Parallel to [001], FeO_4 tetrahedra are arranged into tetrahedral chains by corner-sharing. These chains are in turn connected via corner sharing to form two-dimensional (a–c plane) layers made of ordered six-membered tetrahedral rings (Fig. 2b). (Only a small number of Fe-containing oxides adopt this uncommon ring structure.)[23] Between these layers are a sheet of severely distorted $[BiO_6]^{9-}$ octahedra with four Bi–O bond lengths within 2.130–2.345 Å and the other two at 2.712 Å (Bi–O2) and 2.809 Å (Bi–O3) (Supplementary Table S3). Similarly dispersive metal-oxygen distances are common for Bi^{3+}-containing compounds due to lone pair electrons[24,25]. Along [001] BiO_6 octahedra form zigzag "dimeric" Bi_2O_{10} chains connected by edge sharing (Fig. 2c), which stabilizes the layered structure. Alternating K and Bi in a row along the a-axis maintains an average nominal cation charge of 2+ which further stabilizes the structure by lowering the Coulomb energy. Overall, the structure may be viewed as alternating blocks of $[Fe_2O_3]$ and $[(K, Bi)O_2]$ loosely connected by sharing some corner O (O2, O3, O4 and O5) between FeO_4 and BiO_6 polyhedra. The phase purity of synthesized crystallites was also confirmed by powder XRD, which is identical to the calculated one using single-crystal data (Supplementary Fig. S2). Lastly, transmission electron microscopy (TEM) shows a projected unit cell along the b-axis with
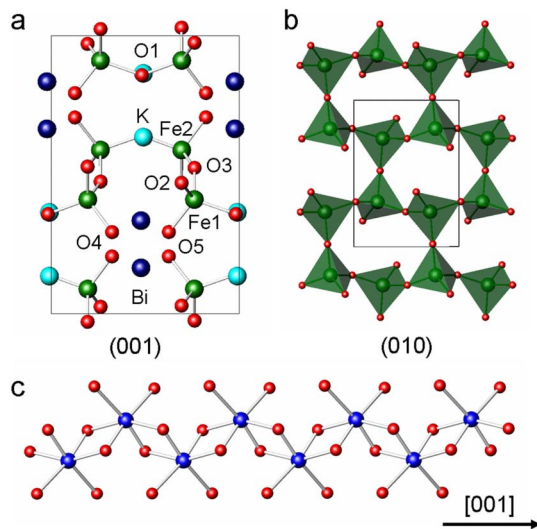

Figure 2 | Crystal structure of $KBiFe_2O_5$ at room temperature, space group $P2_1cn$. (a) Unit cell composition, K (azury), Bi (navy-blue), Fe (green) and O (red). (b) $[Fe_2O_3]$ block viewed along the b-axis. (c) Schematic of dimeric Bi_2O_{10} chains.

cell dimensions and a selected area electron diffraction pattern in agreement with the above structure (Supplementary Fig. S3).

Direct evidence of the noncentrosymmetric nature of the structure ($P2_1cn$) was found in the nonlinear optical response: second-harmonic generation (SHG) was observed when a Q-switched Nd:YAG l064 nm laser light was shone onto a single crystal sample, generating a weak green light of 532 nm (Supplementary Fig. S4). The oxidation states of Fe^{3+} and Bi^{3+} were determined using x-ray photoelectron spectroscopy (XPS) by reference to the binding energies of Fe $2p_{3/2}$ (710.0 eV) and Bi $4f_{7/2}$ (158.3 eV) (Supplementary Fig. S5). The bond valence sums (BVS) gave 2.871 for Bi and 3.079 for Fe. Assuming Fe^{3+} and Bi^{3+} and using the structure in Fig. 2, we calculated the total polarization P_s (the sum of ionic and electronic contributions according to the method reported previously[26]) to be

3.73 µC/cm², with an ionic contribution of 1.47 µC/cm² and an electronic contribution of 2.26 µC/cm². These small polarizations are mainly due to Bi^{3+} and K^+ displacements along [100], which are antiferroelectric-like in the sense that most nearby dipole moments are self-canceling (Supplementary Fig. S6).

Magnetic structure and high temperature transitions. Neutron powder diffraction (NPD) experiments from 4 K to 863 K (Fig. 3 and Supplementary Fig. S7–9 and Table S4–7) were conducted to delineate any structural transition and to clarify magnetic structure. According to the NPD data refinement, there is no structural transition from 4 K to 698 K, although high temperature XRD (Supplementary Fig. S10) did reveal a gradual distortion manifest as some peak splitting culminating in a cell-doubling at about 773 K
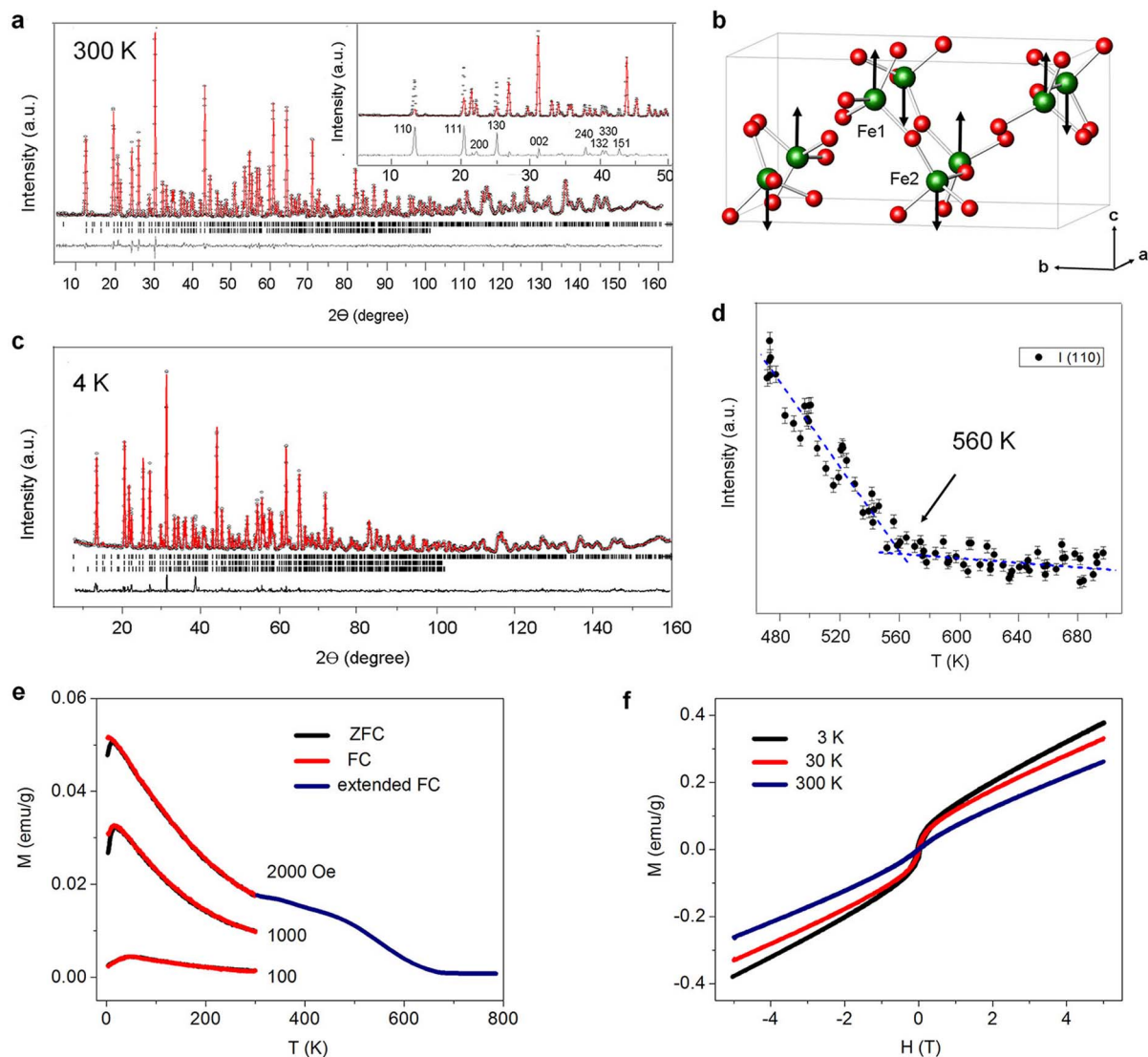

Figure 3 | **Magnetic structure and weak ferromagnetism of KBiFe$_2$O$_5$.** (a) Experimental (circles), calculated (line), and difference ("noise" at bottom) NPD profiles for KBiFe$_2$O$_5$ at 300 K. Vertical bars indicate calculated positions of Bragg peaks from the nuclear phase (upper) and the magnetic phase (lower). $\lambda = 1.5403$ Å. Space group $P2_1cn$, No. 33, $a = 7.9855(1)$ Å, $b = 11.8225(1)$ Å, $c = 5.7396(1)$ Å, $V = 541.87(1)$ Å³; $R_{wp} = 0.0373$, $R_p = 0.0316$, $\chi^2 = 1.230$. Magnetic symmetry of Shubnikov group: $P2_1'cn'$ with Fe moment of 3.77(2) µ$_B$ along c-axis direction. (Inset: Refinement with nuclear phase only. Difference profile shows reflections from magnetic phase). (b) Magnetic and crystal structure of KBiFe$_2$O$_5$ ($P2_1cn$ cell). (c) Experimental (circles), calculated (line), and difference ("noise" at bottom) NPD profiles for KBiFe$_2$O$_5$ at 4 K under 6 T magnetic field. Vertical bars indicate the calculated positions of Bragg peaks from the nuclear phase $P2_1cn$ (upper), from the G-type antiferromagnetic phase $P2_1'cn'$ (lower), and from the ferromagnetic phase $P2_1c'n'$ at 6 T (bottom). $\lambda = 1.5403$ Å. $R_{wp} = 0.0619$, $R_p = 0.0490$, $\chi^2 = 1.348$. (d) Temperature dependence of the magnetic (110) reflection indicative of a magnetic phase transition at ~560 K. (e) Magnetization (M) measured at three fields showing near coincidence of ZFC and FC data except at the lowest temperature at 1 kOe and 2 kOe. Magnetic transition at 2 kOe occurs at about 550 K. (f) Magnetization-field (H) curves at 3 K, 30 K and 300 K.

(space group $Pnna$), which is reminiscent of antiferroelectric structures[27,28]. Finally, above ~848 K $KBiFe_2O_5$ irreversibly transforms to a monoclinic structure (space group $P2/c$) according to both NPD at 863 K (Supplementary Fig. S9) and XRD at 933 K (Supplementary Fig. S10). Such irreversible transition implies that the orthorhombic structure is metastable (no evidence of decomposition was observed from the thermogravimetric analysis given in Supplementary Fig. S11). A similarly irreversible structural transition has been reported in a multiferroic perovskite in which both A site and B site are shared by In and Fe[29].

As shown in Fig. 3a, all peaks of the NPD pattern at 300 K can be indexed to $P2_1cn$, but there are several unaccounted-for peaks especially at low angles (Fig. 3a inset). The intensities of these peaks lessened with temperature suggesting their possible magnetic origin. This was confirmed by magnetic Bragg scattering at 4 K, 5 K and 300 K which identifies the existence of G-type (rock-salt-like antiparallel nearest neighbors) antiferromagnetic order with the magnetic moments along the c-axis (Fig. 3b). However, this spin structure was found to be incommensurate with the structural lattice indicating a small canting of the moments which is the source of weak ferromagnetism not uncommon in oxides with similar G-type ordering[30,31]. Thus, NPD experiments under magnetic field up to 6 Tesla (T) at 4 K (Fig. 3c) were carried out to evaluate the possible ferromagnetism. With the applied vertical magnetic field at as low as 1 T the sample powders started to move and align themselves along the magnetic field, indicating the presence of the ferromagnetism. Rietveld refinement was performed on the data collected at both 0 T and 6 T. At 0 T, only the

G-type antiferromagetic phase was observed with the present instrument resolution. For the 6 T NPD data, besides that G-type antiferromagnetic phase, the ferromagnetic moments was observed with careful data analyses. A magnetic structure model of $P2_1c'n'$ symmetry was proposed and the refinement indicates that the Fe^{3+} has the field induced moment of 0.3(2) μ_B along the a-axis. Consequently, an evidence of the magnetic field induced preferred orientation along the (001) direction was observed, suggesting the presence of the ferromagnetic moment component perpendicular to the c-axis direction (Supplementary Fig. S12). Without the applied magnetic field the refined magnetic moment for Fe is 3.77(2) μ_B at 300 K and 3.87(2) μ_B at 5 K (Supplementary Fig. S7), which is lower than that for a high-spin Fe^{3+} (5.0 μ_B for spin-only contributions). This may be attributed to covalency, low dimensionality of the Fe-O sublattice and perhaps some quantum mechanical effects. Meanwhile, the temperature dependence of the (110) antiferromagnetic reflection (Fig. 3d) indicates a Neel temperature of ~560 K.

Room-temperature magnetic response was found by aligning needle-shaped crystallites of $KBiFe_2O_5$ using a magnet (Supplementary Fig. S13). Consistent with the antiferromagnetic structure, the zero-field-cooled (ZFC) and field-cooled (FC) magnetization of $KBiFe_2O_5$ shown in Fig. 3e have small susceptibility values. They show a very low (spin) freezing temperature that is field sensitive, which supports spin canting and weak ferromagnetism. Weak magnetization was confirmed by M-H hysteresis: at 3 K, 10 K and 300 K as seen in Fig. 3f. The Neel temperature determined by high temperature magnetization measurements (2 kOe, the blue segment in
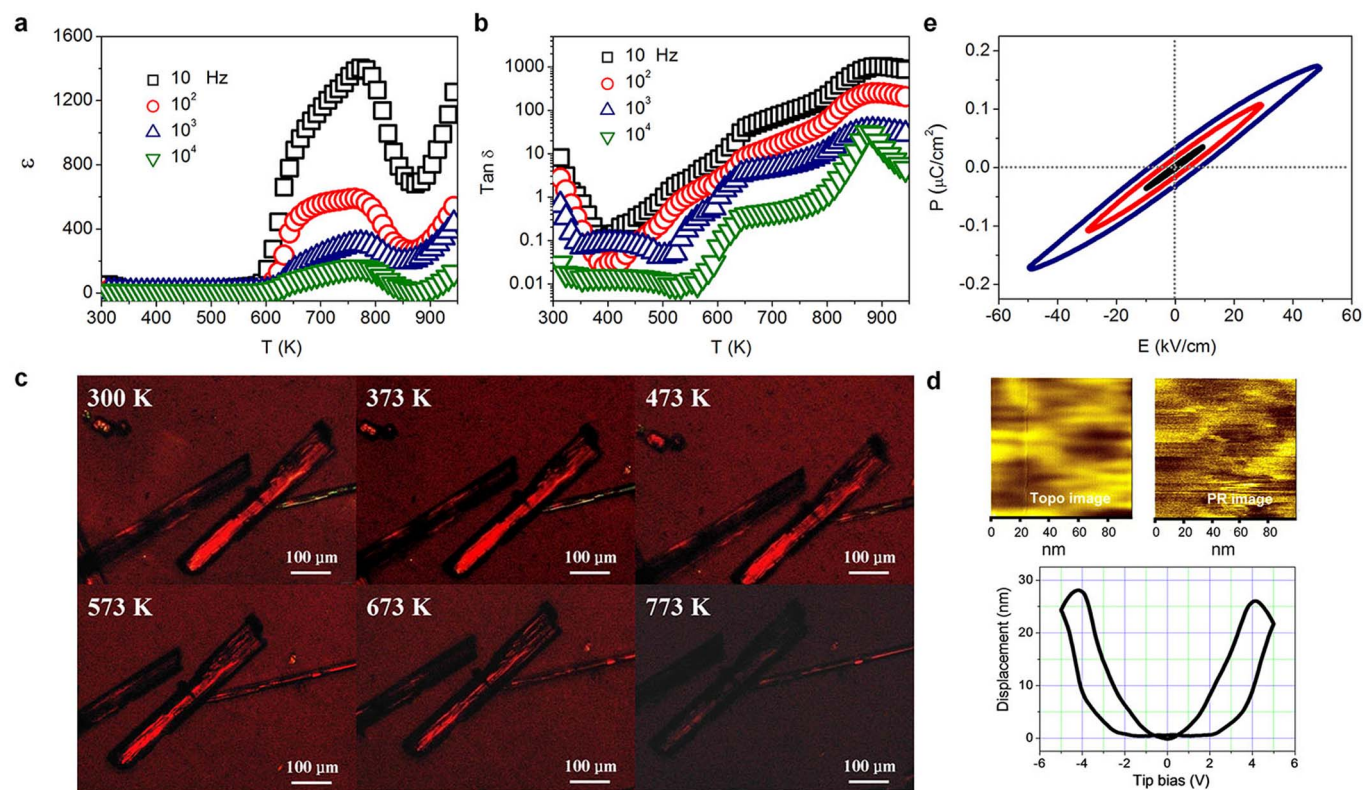

Figure 4 | Electric polarization and phase transition of $KBiFe_2O_5$. (a) Dielectric constant of $KBiFe_2O_5$ as a function of temperature measured at 10^{1-4} Hz, using amplitude of 1 V. (b) Corresponding dielectric loss tangent as a function of temperature. (c) Polarized optical images of $KBiFe_2O_5$ single crystal from room temperature to 773 K showing polarizing light decreasing with temperature and disappearing at 773 K. The transition temperature of 773 K roughly coincides with the cell-doubling transition at 773 K determined by XRD. (d) Topography image (top left) and the corresponding PFM image (top right) along with local piezoelectric response hysteresis loop (bottom) of $KBiFe_2O_5$ single crystal. (e) P-E hysteresis loops measured at room temperature at increasing scan field ranges.

Fig. 3e) was 550 K, which is consistent with NPD results. Since K^+ and Bi^{3+} are both nonmagnetic, these magnetic features must be attributed to the FeO_4 block.

Electric polarization. Inspired by the noncentrosymmetric structure and calculated polarization, we further investigated polarization-related properties. However, it should be noted that, because of the anticipated small bandgap (E_g) of this material, the activation of electronic conduction (with an activation energy $E_g/2$) will intervene complicating the interpretation of the data. First, the temperature and frequency dependence of dielectric constant (ε) and loss tangent (tan δ) was investigated using ceramic sample. The limiting high-frequency (10^4 Hz) dielectric constant at room temperature is 9 suggesting little intrinsic polarizability, yet the temperature dependence of ε and tan δ (Fig. 4a and 4b) is rather rich showing a strong dispersion in that their values decrease sharply with increasing frequency. Below 850 K they may be deconvoluted into two broad intermediate-temperature peaks. (a) A low temperature ε peak at ~640 K (the tan δ rise starting at 500 K). This feature could indicate relaxation of structural polarization (antiferroelectric or antiferromagnetic), onset of Maxwell-Wagner relaxation associated with the onset of electronic conduction divided by insulating internal boundaries, or residual oxygen vacancies similarly reported in other perovskite ferrites[32]. (b) A high temperature peak in ε at 780 K, which roughly coincides with the orthorhombic-to-orthorhombic cell-doubling temperature that is antiferroelectric-like[33,34]. Above 850 K, both ε and tan δ rapidly increase which is most likely due to the (irreversible) phase transition to the monoclinic phase, which may also have increased conductivity. Evidence

for the antiferroelectric-like transition was also observed by differential scanning calorimetry (Supplementary Fig. S14), but more direct evidence for a polarization transition was provided by polarized optical microscopy in Fig. 4c, which shows disappearance of polarized light above 780 K. Lastly, when the stable monoclinic phase formed by heating above 850 K was subsequently cooled, it showed no dielectric anomaly during cooling and reheating between 900 K and room temperature (Supplementary Fig. S15). This indicates that it is paraelectric unlike the low temperature orthorhombic polymorphs, and it is not associated with the antiferroelectric-paraelectric transition. Future work is required to more firmly establish the relation between polarization transition and dielectric spectra.

Further direct evidence of spontaneous polarization switching under an electric field was found in single crystal samples examined using piezoresponse force microscopy (PFM). It revealed a distorted butterfly-like loop of piezoelectric response displacement versus probe tip voltage (Fig. 4d) similar to the electrostriction loops reported in the literature for mixed-phased ferroelectric/antiferro-electric titanates[35,36]. Contrasts (presumably due to domains of opposite polarization) were also seen in PFM of the same region. The polarization (P)-field (E) loops of single-crystal samples measured at room temperature (Fig. 4e) feature small, field-reversible remnant polarization consistent with the small calculated values, but loop saturation was not achieved because the high (coercive) field required for saturation could not be applied due to leakage-caused breakdown. (Incidentally, this is expected to be a general problem for low E_g FE tailored to the photovoltaic applications[12,37]. Even in $BiFeO_3$ which has a higher E_g, efforts to increase its conductivity to
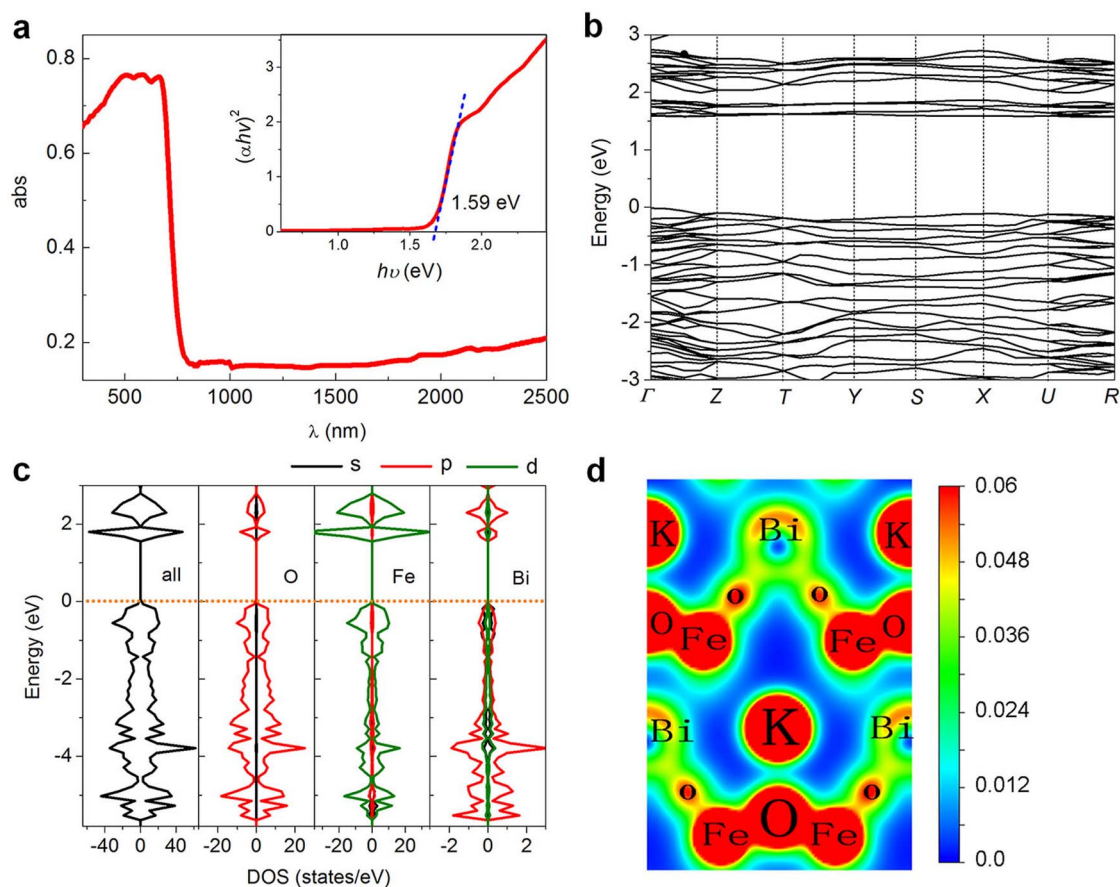

Figure 5 | Band structure of $KBiFe_2O_5$. (a) UV-Vis-near IR absorption spectrum of $KBiFe_2O_5$. Inset: $(\alpha h\nu)^2$ versus $h\nu$ for band gap determination. (b) Band structure of $KBiFe_2O_5$, (c) Spin-up (left branch) and spin-down (right branch) components of density of states (DOS), and (d) charge density parallel to the 001 plane.

improve photovoltaic responses inevitably render it impossible for manifesting saturated *P-E* loops[38–40]). Taken into account the structural, dielectric, piezoelectric and remnant polarization data, we may conclude that the low temperature orthorhombic phase is a canted FE, which probably transforms to an antiferroelectric orthorhombic phase above 780 K and finally to a paraelectric-like monoclinic phase above 850 K.

Band structure. Our expectation of a smaller E_g and a higher conductivity for tetrahedral compounds was supported by optical absorption spectrum (Fig. 5a) which shows increased absorption starting at 750 nm. Using the plot of photon energy *hν* versus $(\alpha h\nu)^2$ (α for absorbance), we extrapolated an absorption edge of 1.59 eV which corresponds to the optical band gap (Fig. 5a inset). This value is considerably lower than that of $BiFeO_3$ and is near the optimal band gap (1.50 eV) for solar energy applications. The smaller E_g is consistent with a lower resistance: the room-temperature resistance of the single sample obtained from the dark Current-voltage measurement discussed later is about 0.96×10^7 Ω·cm, which is three orders of magnitude lower than that of $BiFeO_3$. Moreover, the large light absorption coefficient of the sample was detected as $> 10^4$ cm^{-1} (Supplementary Fig. S16), which is suitable for solar energy application.

To gain insight to the band structure, first-principles electronic band structure calculations were performed. They revealed a direct band gap (about 1.58 eV) at the Γ (0.0, 0.0, 0.0) point (Fig. 5b) between a valence band maximum of mostly O $2p$ character and a conduction band minimum of mostly Fe $3d$ character (Fig. 5c), which agrees with the measured optical E_g. Such a direct transition

from isocentered Fe $3d^5$ favors to a large light absorption coefficient for the material. Charge density along the 100 plane shows considerable in-plane Fe–O bonding next to K, whereas Bi–O bonding is primarily off the plane (Fig. 5d). The relatively low dimensionality of Fe–O bonding appears to be an important factor in the small E_g in this compound.

Photoelectric responses. The photoelectric responses were measured at room temperature using a single crystal illuminated by a UV-light (4 mW/cm², λ ~ 254 nm) (see insert in Fig. 6a and Supplementary Fig. S17). Current–voltage (I–V) characteristics of samples reveal strikingly photovoltaic behavior, which is indicative of the polar nature of the sample. At zero bias, no dark current was seen but there is a negative photocurrent, with a large zero-current voltage (corresponding to the open-circuit photovoltaic voltage, V_{oc}) of 8.8 V (Fig. 6a). This indicates that charge carriers have a preferred direction presumably because of an internal-field bias. The observation of an open circuit voltage larger than E_g is a signature of photovoltaic effects in multi-domained FE[4,10]. This above band gap V_{oc} provides a promising platform for harvesting solar energy to generate electricity. These results provided strong evidence for the presence of a FE bias in the crystal. To substantiate the above results and to eliminate any heating effect caused by sustained light illumination, on-off photocurrent at zero voltage and V_{oc} at zero current were measured (Fig. 6b and 6c), which again confirmed the photoelectric effect. A steady V_{oc} was obtained as large as 9.1 V, which is consistent with the I–V result. The photocurrent density ~15 µA/cm² is comparable to the one (7.35 µA/cm²) reported for $BiFeO_3$[12]. Note that our photovoltaic effect was measured from one single crystal
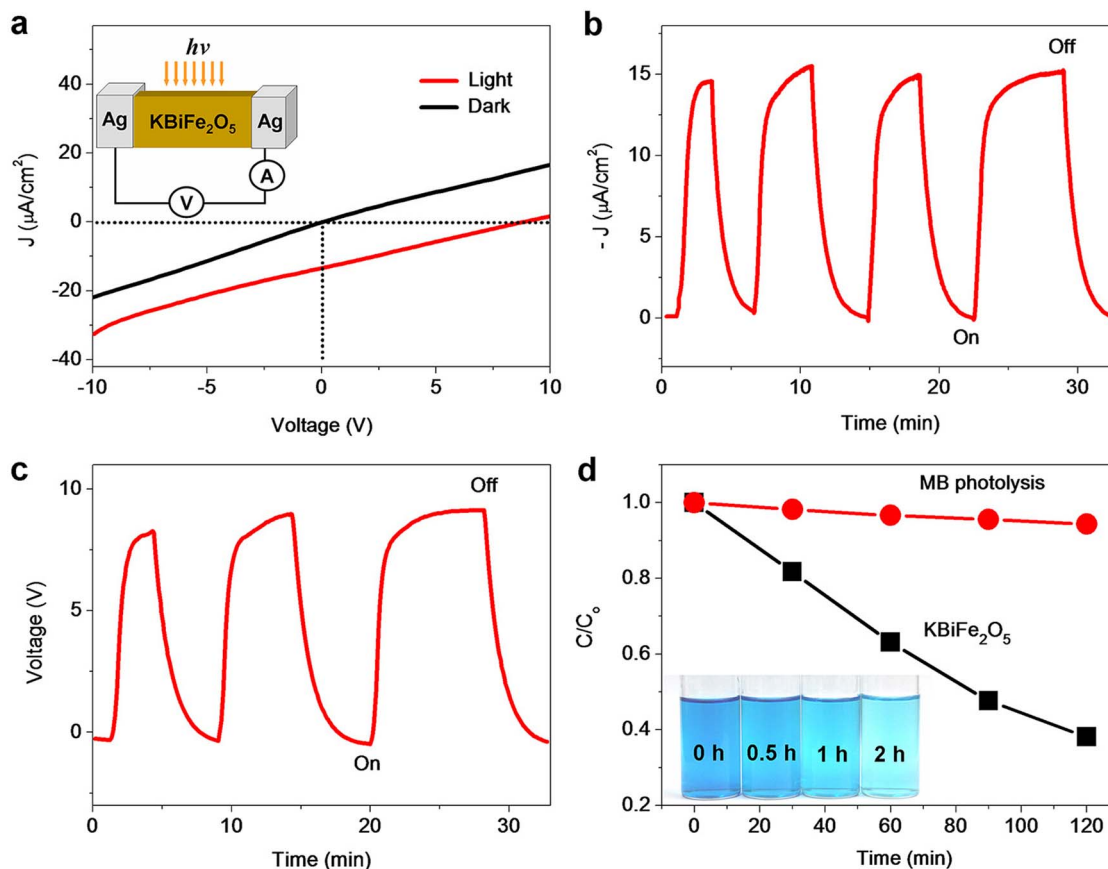

Figure 6 | Photoelectric Responses of KBiFe$_2$O$_5$. (a) *J-V* curves in the dark and under UV illumination at room temperature. Inset shows the measurement setup schematically. (b) Zero-voltage photocurrent density following on-off UV exposure. (c) Open-circuit photovoltaic voltage following on-off UV exposure. (d) Photocatalytic decoloration of methylene blue (MB) under visible light with (lower) and without (upper) KBiFe$_2$O$_5$ powders. Inset: color evolution of MB at corresponding irradiation time.

sample whose photovoltaic efficiency is considerably limited. Photocurrent is known to be sensitive to the illumination condition and device configuration[4,39,40], so a major enhancement in its value is possible by modifying these parameters and by tuning conductivity.

Further evidence of photon-generated carriers in $KBiFe_2O_5$ came from photocatalytic activity. Under visible light illumination (light source: VIS 300 W Xe lamp, filter: $\lambda = 420$ nm), methelene blue (MB) dye was reduced to 50% of its initial concentration ($C_0 \sim 1 \times 10^{-5}$ mol L^{-1}) in 80 min (Fig. 6d) in the presence of $KBiFe_2O_5$ powders compared to less than 0.06% if without. The increased degradation may be attributed to electron donation from $KBiFe_2O_5$ as a photocatalyst. Together, these results leave no doubt that there are robust photoelectric effects in polar, orthorhombic $KBiFe_2O_5$.

Discussion

Herein, we have discovered a high T_c, small band gap (1.6 eV), weakly ferroelectric and ferromagnetic compound, $KBiFe_2O_5$, as a member of the tetrahedrally coordinated $A_2B_2O_5$ structural family, which has many attributes suitable for solar energy applications. It provides the first evidence that inherently polar compounds made of transition metal MO_4 tetrahedral network structures can offer smaller band gaps than conventional ferroelectrics, thus higher light absorption and carrier concentrations facilitating solar energy conversion. This discovery should encourage further exploration of tetrahedral structured compounds as a new class of polar, photoactive functional materials.

Methods

$KBiFe_2O_5$ single crystal growth. In a typical synthesis procedure for $KBiFe_2O_5$, 15 mL $Bi(NO_3)_3$ (0.2 M) and 30 mL $Fe(NO_3)_3$ (0.2 M) were initially mixed in a beaker by continuous stirring. To this, 50 g KOH was added under stirring and the solution was allowed to cool to the room temperature. The mixture was then transferred into a 100-mL Teflon-lined stainless steel autoclave to fill 70% of its capacity. Crystallization was carried out under autogenous pressure at 220°C for 3 days. After the autoclave was cooled and depressurized, product was washed (with distilled water), sonicated and harvested as a fine, dark brown crystallite sediment.

Crystal structure characterization. A relatively large, good quality single crystal was analyzed at room temperature by X-ray diffraction (XRD) using an Enraf-Nonius Kappa CCD diffractometer with graphite-monochromatized Mo $K\alpha$ ($\lambda = 0.71073$ Å) radiation following the ω-2θ scan method. The absorption correction was applied using the SADABS program[41]. The structure was solved by the direct method and refined on F^2 by the full-matrix least-square method using the SHELXS-97 and SHELXL-97 programs, respectively[42,43]. Cation atoms were first located, then oxygen atoms were found in a difference Fourier map.

NPD data from 5 K to 863 K were collected at the NIST Center for Neutron Research (NCNR) using the BT-1 high-resolution neutron powder diffractometer with a Cu(311) monochromator at $\lambda = 1.5403$ Å. All crystal structures were solved by direct-space method. Rietveld structural refinements were performed on the resulting models using GSAS package[44,45]. Powder XRD data of the same samples were also collected from room temperature to 933 K on a Rigaku D/Max-2000 diffractometer with Cu K radiation ($\lambda = 1.5418$ Å with a graphite monochromator) at 40 kV and 100 mA.

Inductively couple plasma (ICP) analysis carried out on a PROFILE SPEC ICP instrument gave a K : Bi : Fe ratio of 0.98 : 1.02 : 2.00. The oxidation states of Fe and Bi were investigated by X-ray photoelectron spectroscopy (XPS) using an Axis Ultra spectrometer. The spectra collected for the C 1s, Fe 2p, Bi 4f and O 1s regions with binding energies were corrected against the C 1s reference of 284.5 eV. Thermogravimetric (TG) and Differential Thermal Analysis (DTA) were carried out on a Netzsch STA449C (Germany) thermal analyzer. Differential scanning calorimetry (DSC) measurements were performed on a DSC-Q100 differential scanning calorimeter (TA Instruments Inc.).

UV-Vis-near IR absorption spectra were recorded on a UV-3100 Shimadzu ultraviolet-visible-infrared spectrophotometer. Single crystals were examined in a Polarizing Optical Microscope (Leica DM LP) in the temperature range from room temperature to 823 K at a heating rate of 20 K/min. In addition, sample morphology and microstructure were investigated by scanning electron microscopy (SEM, performed on a FEI Quanta 200F microscope operating at 3 KV) and transmission electron microscopy (TEM, carried out on a JEM2100F with an accelerating voltage of 200 kV).

Density functional calculation. To determine band structures, the projector augmented wave (PAW) method was used in the density-functional theory (DFT) calculations, which included the PBE version of the generalized gradient approximation (GGA) to describe the exchange correlation functional[46,47]. Here, the

cutoff energy of plane wave was chosen at 350 eV. For Brillouin zone integration, $4 \times 2 \times 6$ Γ-centered Monkhorst–Pack grids were performed.

Magnetic and electric properties characterization. Magnetic properties were studied using a Quantum Design physical properties measurement system (PPMS). DC susceptibility was measured under zero-field-cooling (ZFC) and field-cooling (FC) conditions in several magnetic fields from 2 to 320 K; a high temperature measurement (300~800 K) under 2 kOe was also conducted. Dielectric properties of ceramics were measured using a Precision Impedance Analyzer 65120B (Wayne Kerr Electronics) between 300 and 850 K in the frequency range from 10 to 10^4 Hz. For dielectric measurements, ceramic samples were prepared by packing ground powders (crystallites) in a wrapped gold foil, followed by hot pressing at 6 GPa and 800 K for 6 h inside a CS-IV 6×14 MN cubic press (the High-Pressure Laboratory, Peking University)[48]. The obtained ceramics have a density of 5.265 g/cm³, which is about 97.6% of the theoretical value (5.394 g/cm³). Their XRD pattern is identical to that of the starting powders (Supplementary Fig. S18). Before dielectric testing, the gold foils at the side of the ceramic sample were polished away while the gold foils at the top and bottom surfaces were kept as the electrodes. Single-crystal polarization test devices were made by painting Ag electrodes onto two opposing sides of the crystals as shown in Fig. S17. Polarization–electric field (P–E) hysteresis loops of single-crystal samples were investigated using an aixACCT FE test unit (Aachen, Germany) with probes on the electrodes of the samples, which were immersed in silicone oil to prevent arcing. Piezoresponse force microscopy (PFM) characterization at room temperature was conducted in an atomic force microscope using a tip-cantilever system (NSC35/ Ti–Pt, MicroMasch) with a spring constant of 14 N·m^{-1}. Domain visualization was performed under an externally applied ac voltage with an amplitude $V_{ac} = 5$ V and a frequency $f = 6.5$ kHz. Conductivity (J-E) measurements were performed by sweeping the voltage from the positive maximum to the negative maximum using a semiconductor characterization system (KEITHLEY 4200).

1. Glass, A. M., Von der Linde, D. & Negran, T. J. Highvoltage bulk photovoltaic effect and the photorefractive process in LiNbO₃. *Appl. Phys. Lett.* **25**, 233 (1974).
2. Dalba, G., Soldo, Y., Rocca, F., Fridkin, V. M. & Sainctavit, Ph. Giant bulk photovoltaic effect under linearly polarized X-Ray synchrotron radiation. *Phys. Rev. Lett.* **74**, 988 (1995).
3. Yang, Y. S., Lee, S. J., Yi, S., Chae, B. G. & Lee, S. H. Schottky barrier effects in the photocurrent of sol–gel derived lead zirconate titanate thin film capacitors. *Appl. Phys. Lett.* **76**, 774 (2000).
4. Yang, S. Y. *et al.* Above-bandgap voltages from ferroelectric photovoltaic devices. *Nature Nanotech.* **5**, 143–147 (2010).
5. Kundys, B., Viret, M., Colson, D. & Kundys, D. O. Light-induced size changes in BiFeO₃ crystals. *Nature Mater.* **9**, 803–805 (2010).
6. Yuan, Y. *et al.* Efficiency enhancement in organic solar cells with ferroelectric polymers. *Nature Mater.* **10**, 296–302 (2011).
7. Choi, W. S. *et al.* Wide bandgap tunability in complex transition metal oxides by site-specific substitution. *Nature Commun.* **3**, 689 (2012).
8. Inoue, Y., Sato, K. & Miyama, H. Photoassisted water decomposition by ferroelectric lead zirconate titanate ceramics with anomalous photovoltatic Effects. *J. Phys. Chem.* **90**, 2809–2810 (1986).
9. Fridkin, V. M. Bulk photovoltaic effect in noncentrosymmetric crystals. *Crystallogr. Rep.* **46**, 654–658 (2001).
10. Seidel, J. *et al.* Efficient photovoltaic current generation at ferroelectric domain walls. *Phys. Rev. Lett.* **107**, 126805 (2011).
11. Würfel, P. *Physics of Solar Cells.* (Wiley, Weinheim, 2009).
12. Choi, T., Lee, S., Choi, Y. J., Kiryukhin, V. & Cheong, S.-W. Switchable ferroelectric diode and photovoltaic effect in BiFeO₃. *Science* **324**, 63–66 (2009).
13. Basu, S. R. *et al.* Photoconductivity in BiFeO₃ thin films. *Appl. Phys. Lett.* **92**, 091905 (2008).
14. Lebeugle, D. *et al.* Room-temperature coexistence of large electric polarization and magnetic order in BiFeO₃ single crystals. *Phys. Rev. B* **76**, 024116 (2007).
15. Bennett, J. W., Grinberg, I. & Rappe, A. M. New highly polar semiconductor ferroelectrics through d^8 cation-O vacancy substitution into PbTiO₃: A theoretical study. *J. Am. Chem. Soc.* **130**, 17409–17412 (2008).
16. Bennett, J. W., Grinberg, I., Davies, P. K. & Rappe, A. M. Pb-free semiconductor ferroelectrics: A theoretical study of Pd-substituted Ba(Ti$_{1−x}$Ce$_x$)O₃ solid solutions. *Phys. Rev. B* **82**, 184106 (2010).
17. Qi, T., Grinberg, I. & Rappe, A. M. Band-gap engineering via local environment in complex oxides. *Phys. Rev. B* **83**, 224108 (2011).
18. D'Hondt, H. *et al.* Tetrahedral chain order in the Sr₂Fe₂O₅ brownmillerite. *Chem. Mater.* **20**, 7188–7194 (2008).
19. Shaula, A. L. *et al.* Ionic conductivity of brownmillerite-type calcium ferrite under oxidizing conditions. *Solid State Ionics* **177**, 2923–2930 (2006).
20. Peterson, S. W., Levy, H. A. & Simonsen, S. H. Neutron diffraction study of the ferroelectric modification of potassium dihydrogen phosphate. *Phys. Rev.* **93**, 1120–1121 (1954).
21. Iwasaki, H., Miyazawa, S., Koizumi, H., Sugii, K. & Niizeki, N. Ferroelectric and optical properties of Pb₅Ge₃O₁₁ and its isomorphous compound Pb₅Ge₂SiO₁₁. *J. Appl. Phys.* **43**, 4907–4915 (1972).
22. Palewicz, A., Sosnowska, I., Przeniosło, R. & Hewat, A. W. BiFeO₃ crystal structure at low temperatures. *Acta Phys. Pol. A* **117**, 296–301 (2010).

23. Zhao, Q. *et al.* Ba$_4$KFe$_3$O$_9$: A novel ferrite containing discrete 6-membered rings of corner-sharing FeO$_4$ tetrahedra. *Inorg. Chem.* **50**, 10310–10318 (2011).

24. Yang, J. & Dolg, M. First-Principles Electronic structure study of the monoclinic crystal bismuth triborate BiB$_3$O$_6$. *J. Phys. Chem. B* **110**, 19254–19263 (2006).

25. Chen, X. *et al.* Synthesis and crystal structure of a novel ternary oxoborate, PbBiBO$_4$. *J. Solid State Chem.* **179**, 3191–3195 (2006).

26. Bruyer, E. & Sayede, A. Density functional calculations of the structural, electronic, and ferroelectric properties of high-k titanate Re$_2$Ti$_2$O$_7$ (Re = La and Nd). *J. Appl. Phys.* **108**, 053705 (2010).

27. Dorcet, V., Trolliard, G. & Boullay, P. Reinvestigation of Phase Transitions in Na$_{0.5}$Bi$_{0.5}$TiO$_3$ by TEM. Part I: First order rhombohedral to orthorhombic phase transition. *Chem. Mater.* **20**, 5061–5073 (2008).

28. Mishra, K., Choudhury, N., Chaplot, S. L., Krishna, P. S. R. & Mittal, R. Competing antiferroelectric and ferroelectric interactions in NaNbO$_3$: Neutron diffraction and theoretical studies. *Phys. Rev. B* **76**, 024110 (2007).

29. Belik, A. A. *et al.* Indium-Based Perovskites: A new class of near-room-temperature multiferroics. *Angew. Chem. Int. Ed.* **48**, 6117–6120 (2009).

30. Ramezanipour, F. *et al.* Intralayer cation ordering in a brownmillerite superstructure: synthesis, crystal, and magnetic structures of Ca$_2$FeCoO$_5$. *Chem. Mater.* **22**, 6008–6020 (2010).

31. Seddon, J., Suard, E. & Hayward, M. A. Topotactic reduction of YBaCo$_2$O$_5$ and LaBaCo$_2$O$_5$: Square-planar Co(I) in an extended oxide. *J. Am. Chem. Soc.* **132**, 2802–2810 (2010).

32. Ma, Y. & Chen, X. M. Enhanced multiferroic characteristics in NaNbO$_3$-modified BiFeO$_3$ ceramics. *J. Appl. Phys.* **105**, 054107 (2009)

33. Chen, I. W. Structural origin of relaxor ferroelectrics—revisited. *J. Phys. Chem. Solids* **61**, 197–208 (2000).

34. Sigman, J., Norton, D.P., Christen, H. M., Fleming, P.H. & Boatner, L.A. Antiferroelectric Behavior in Symmetric KNbO$_3$KTaO$_3$ Superlattices. *Phys. Rev. Lett.* **88**, 097601 (2002).

35. Guo, Y., Liu, Y., Withers, R. L., Brink, F. & Chen, H. Large electric field-induced strain and antiferroelectric behavior in (1-x)(Na$_{0.5}$Bi$_{0.5}$)TiO$_3$-xBaTiO$_3$ ceramics. *Chem. Mater.* **23**, 219–228 (2011).

36. Zhang, S. *et al.* Lead-free piezoceramics with giant strain in the system Bi$_{0.5}$Na$_{0.5}$TiO$_3$–BaTiO$_3$–K$_{0.5}$Na$_{0.5}$NbO$_3$. I. Structure and room temperature properties. *J. Appl. Phys.* **103**, 034107 (2008).

37. Lee, W. *et al.* Spatially resolved photodetection in leaky ferroelectric BiFeO$_3$. *Adv. Mater.* **24**, OP49–OP53 (2012).

38. Balke, N. *et al.* Enhanced electric conductivity at ferroelectric vortex cores in BiFeO$_3$. *Nature Phys.* **8**, 81–88 (2011).

39. Yang, X. *et al.* Enhancement of photocurrent in ferroelectric films via the incorporation of narrow bandgap nanoparticles. *Adv. Mater.* **24**, 1202–1208 (2012).

40. Alexe, M. & Hesse, D. Tip-enhanced photovoltaic effects in bismuth ferrite. *Nature Commum.* **2**, 256 (2011).

41. Sheldrick, G. M. *SADABS. Version 2007/2* (Bruker AXS Inc., Madison, Wisconsin, USA, 2007).

42. Sheldrick, G. M. *SHELXS97, Program for Solution of Crystal Structures* (University of Göttingen, Göttingen, Germany, 1997).

43. Sheldrick, G. M. *SHELXL97, Program for Solution of Crystal Structures* (University of Göttingen, Göttingen, Germany, 1997).

44. Larson, A. C. & Von Dreele, R. B. *General Structure Analysis System (GSAS)* (Los Alamos National Laboratory Report LAUR 86–748, 2000).

45. Toby, B. H. EXPGUI, a graphical user interface for GSAS. *J. Appl. Cryst.* **34**, 210–213 (2001).

46. Perdew, J. P., Burkeand, K. & Ernzerhof, M. Generalized gradient approximation made simple. *Phys. Rev. Lett.* **77**, 3865 (1996).

47. Blöchl, P. E. Projector augmented-wave method. *Phys. Rev. B* **50**, 17953–17979 (1994).

48. Liu, X. *et al.* A large volume cubic press with a pressure-generating capability up to about 10GPa. *High Press. Res.* **iFirst**, 1–16 (2012).

Author contributions

F.Q.H. and J.H.L conceived the idea and designed the experiments. G.H.Z performed the experiments and measurements. H.W. and Q.Z.H. were responsible for the NPD measurement and data analysis. G.B.L. analyzed the single-crystal XRD data. F.Q.H. and G.H.Z. co-wrote the paper. J.H.L. reviewed and commented on the paper. All authors discussed the results and commented on the manuscript.

Additional information

Supplementary information accompanies this paper at http://www.nature.com/scientificreports

Competing financial interests: The authors declare no competing financial interests.

How to cite this article: Zhang, G.H. *et al.* New high T_c multiferroics KBiFe$_2$O$_5$ with narrow band gap and promising photovoltaic effect. *Sci. Rep.* **3**, 1265; DOI:10.1038/srep01265 (2013).